Local degradation analysis of a real long-term operated DMFC stack MEA

Peter Hartmann, Dietmar Gerteisen*

Department of Energy Technology, Fraunhofer Institute for Solar Energy Systems, Heidenhofstrasse 8, 79110 Freiburg, Germany

HIGHLIGHTS

► Local degradation of a long-term operated DMFC MEA is analyzed.
► Anode and cathode losses via reference electrode measurements are separated.
► Relaxation behaviour after CI are correlated with methanol crossover/CO poisoning.
► Degradation is not correlated with the flow field pattern.

ABSTRACT

Understanding degradation of the membrane–electrode assembly (MEA) of direct methanol fuel cells (DMFC) is important technically and scientifically for the advancement of this technology. In this work, we carry out a spatially resolved investigation of the degradation of an MEA, which has been degraded through its operation lifetime. The MEA has an active area of 320 cm^2 and has been used in operation of a DMFC stack for more than 3000 h to power a lift truck. The analysis of degradation with respect to the local position of the flow field pattern was carried out by cutting the MEA into small pieces that are characterized in a 1 cm^2 sized test cell with a reference electrode setup. The characterization techniques involved measurement of anode and cathode polarization curves, electrode potential relaxation curves after current interruption, MeOH-stripping voltammograms, cyclic voltammetry and SEM/EDX analysis. The MEA pieces were prepared by Laser ablation technique to realize the reference electrodes. The analysis yielded an independence of performance from the local position of the MEAs within the stack in terms of the anode and cathode flow fields.

© 2012 Elsevier B.V. All rights reserved.

1. Introduction

Growing concerns about energy shortage and climate change raise the question of an alternative to our oil based economy. One promising concept is the so-called Methanol-Economy promoted by Olah et al. [1]. Methanol serves as a renewable energy source gained out of, e.g., biomass. The high energy density of liquid methanol, simple storage compared to hydrogen, fast refuelling, low operating temperatures and no need of a reformer provide direct methanol fuel cells (DMFCs) with the potential to outperform other fuel cells. Nevertheless, improving the performance and long-term stability are the key factors for success of DMFCs in the market.

As different phenomena are involved in the current generation of a DMFC (charge transfer reaction, mass transport, adsorption processes, etc.), the measured performance loss due to degradation

of the membrane–electrode assembly (MEA) can be the result of various causes. In general, the main degradation phenomena within a DMFC MEA can be categorized into eight different processes. (1) Pt surface oxidation at the cathode [2–5] is reported to decrease the electrocatalytic activity for oxygen reduction. It can be investigated via the oxide reduction peak of cyclovoltammetry measurements. (2) Ruthenium crossover from the anode to the cathode [6–8] results mainly in a fuel cell performance loss due to a more sluggish oxygen reduction reaction on Pt–Ru alloys at the cathode compared to pure platinum. Ex-situ EDX analysis can be used to examine ruthenium at the cathode. CO stripping scan is an in-situ technique to investigate the presence of Ru at the cathode [9,10]. Chen et al. [10] and Choi et al. [9] found a decreasing onset and peak potential with operation time. They argued that the increasing amount of Ru lowers the potential for CO oxidation compared to a pure platinum electrode. (3) Catalyst particle growth [11] also leads to a lower electrochemical active surface area. It can be determined with ex-situ techniques, such as TEM and XRD measurements. (4) Electrochemical corrosion of carbon support at the cathode side [12] results in a loss of electrochemical active

surface area and a decrease of cathode kinetics, which is measured by using in-situ EQCM. (5) Hydrophobicity loss of the cathode gas diffusion layer (GDL) [13] leads to water accumulation and a blockage of the reaction sites. Decreasing hydrophobicity results in a smaller contact angle of the water droplet on the GDL fibres measured by the Sessile-drop method. (6) In solutions with high methanol concentration, significant membrane thinning was observed [14], due to the fact that Nafion® is solvable in methanol. This leads to increased methanol crossover and strong mixed-potential formation on the cathode. (7) The presence of foreign cationic ions can significantly decrease cell performance by adsorbing on the membrane due to a decreased proton conductivity [15]. (8) Membrane–electrode interface delamination occurs primarily at the DMFC anode [16,17] and results in an increase of the interfacial resistance.

Although much work has already been done on the degradation of DMFC MEAs, it has been mostly carried out for a controlled MEA degradation in the lab with a fuel cell of non-technical relevant size. In this work, we investigate the local degradation of an MEA operated in a DMFC stack under real operating conditions. This type of analysis is important to establish an understanding of the degradation of the cell in an actual system. The degradation is examined by polarization curves, electrode overpotentials, current interruption measurements, methanol stripping voltammograms, cyclic voltammetry and SEM/EDX analysis. An identical stack MEA to that used in this work was examined by Dixon et al. [18] to analyze local catalyst degradation using different ex-situ techniques, such as EDX, TEM, XAS, XRD. Hence, this work complements that of Dixon et al. by studying the local degradation via various in-situ electrochemical techniques and SEM/EDX.

2. Experimental

2.1. MEA preparation and test cell

The MEA tested in this study was in operation for more than 3000 h within a stack consisting of 90 cells. Hence, the MEA has been exposed to various degradation mechanisms during its operation lifetime from alternating voltage operations to stop and start conditions. The average current density during load was between 50 and 100 mA cm^{-2} and the average cell temperature ranged from 50 to 70 °C. Each MEA has an active area of 320 cm^2 and consists of seven layers. A Nafion® 115 membrane is used as the electrolyte membrane. Pt–Ru serves as anode catalyst with a loading of 3.0 mg Pt cm^{-2} and 1.5 mg Ru cm^{-2}. The cathode catalyst is Pt with a loading of 1.5 mg cm^{-2}. At both electrodes there is a micro porous layer (MPL) between the catalyst layer (CL) and the gas diffusion layer (GDL). In order to carry out spatially resolved measurements, the MEA was cut into pieces that fit into a test cell with a geometric active area of 1 cm^2. The segmentation was arranged with respect to the anode flow field pattern (multiple-serpentine) of the DMFC stack (see Fig. 1). The cathode flow field of the stack has a parallel structure and was operated in counter-flow mode. By means of Laser ablation technique a 300 μm wide gap is simultaneously implemented on both electrodes, anode and cathode. This results in an electrically isolated part on the electrodes within the reactant compartment, which serves as a reference electrode. Details of the test cell, test bench and the use of Laser ablation technique for preparing reference electrodes are given in [19]. For the characterization work, the educts first pass the reference electrodes before they enter the flow field of the test cell. This configuration keeps the influence of the operating conditions on the educts' properties (concentration, temperature, humidity, flow) on the reference electrode potential low. The reference electrodes were under load via a 10 Ω resistance to further improve
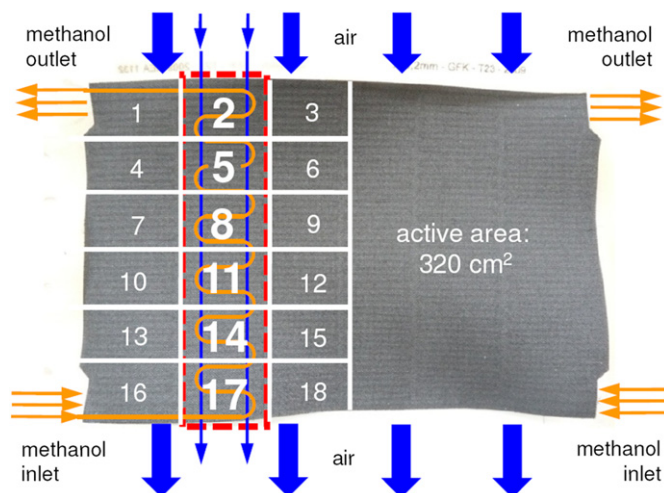

Fig. 1. MEA with segmentation aligned to the anode flow field. Characterized segments are 2, 5, 8, 11, 14 and 17. Methanol inlet: segment 17, methanol outlet: segment 2.

their stability. All voltage measurements concerning the reference potential were done by the oxygen-driven reference electrode. Selected MEA pieces (2, 5, 8, 11, 14, 17) with respect to the flow field configuration within the stack, see Fig. 1, were individually analyzed by several in-situ characterization techniques at the same operating conditions.

2.2. Operating conditions

The same operating conditions were used for each segment. The operating conditions listed in Table 1 have been kept constant unless otherwise stated in the text. Directly before starting the characterization measurements, a standardized preconditioning of the respective MEA sample by load cycles and idling periods of a total duration of 20 h was used to activate the electrodes and rehydrate the membrane. Additionally, benchmark measurements of a new (not operated) MEA of a similar manufactured batch were conducted to have reference data compared to the degraded MEAs. The new MEA was preconditioned for around 40 h with the same protocol as the degraded MEA.

2.3. Characterization techniques

2.3.1. Polarization curve measurements

Using a reference electrode configuration enables the investigation of the anode and cathode separately. The polarization curves were conducted in potentiostatic mode. Starting from open circuit voltage (OCV), the cell voltage was stepwise lowered up to 50 mV, using voltage steps of 50 mV. Every step was held for one minute to reach a quasi steady state. The last 80% of the recorded current density data at each voltage step was averaged to get a single

Table 1
Operating conditions of the characterization measurements.

Concentration of the methanol–water-solution	1 M
Volume flow of the methanol–water-solution	0.8 ml min^{-1}
Volume flow of the air	37 ml min^{-1}
Pressure at the cathode	1150 mbar
Cell temperature	70 °C
Temperature of the inlet gas at the cathode side	70 °C
Dew point of the humidified air	65 °C
Clamping pressure between flow field and MEA	0.78 N mm^{-2}

current density value, j, for each voltage set point. The overpotential of anode, η_a, and cathode, η_c, are related to the cathode reference potential ($\varphi_{c,ref}$) in the following way

$$\eta_{a/c}[j] = +/-\left(\phi_{a/c}[j] - \phi_{c,ref}\right) -/+ \left(\phi_{a/c}[j=0] - \phi_{c,ref}\right) \qquad (1)$$

where $\varphi_{a/c}$ is the anode and cathode potential, respectively.

2.3.2. Current interrupt measurements

The current interrupt measurements were achieved by operating the MEA at a specific load current until steady state was reached. The load was then immediately dropped off and the relaxation curve of the cell voltage, the anode and cathode potential were recorded. This was done for current densities starting from 50 mA cm^{-2} to 400 mA cm^{-2} in 50 mA cm^{-2} steps. Usually current interrupt measurements are used to determine the ohmic resistance of the cell. In this work, however, the data were used to investigate the transient behaviour of the electrode potentials in a time range of seconds where methanol permeation through the membrane and adsorption processes on the catalyst sites are relevant [20].

Since this measurement technique is not common in fuel cell diagnostic, some fundamentals are given here in more detail. The characteristics of the cathode relaxation curve after current interruption is dominated by the interplay of the oxygen reduction reaction (ORR) that pushes the electrode potential to the high equilibrium potential of the ORR and the methanol oxidation reaction (MOR) of permeated methanol on the cathode that forces the electrode potential towards the low MOR equilibrium potential. The amount of methanol concentration on the cathode side determines the steady-state potential at which the ORR can counterbalance the parasitic MOR. Since the methanol flux through the membrane, and therefore the methanol concentration on the cathode, depends on the methanol consumption in the anode catalyst layer, the methanol concentration on the cathode increases with time after CI. By assuming simplified reaction kinetics of the ORR and MOR, expressed by a Tafel approach, the characteristics of the cathode overpotential, η_C, can be described as follows

$$C_{DL}\frac{\partial \eta_c}{\partial t} = i^0_{ORR}C_{O_2}e^{\frac{\eta_c}{b_{ORR}}} - i^0_{MOR}C_{MeOH}e^{\frac{\tilde{\eta}-\eta_c}{b_{MOR}}} \qquad (2)$$

The first term on the right-hand side describes the ORR and the second term describes the MOR with $i^0_{ORR/MOR}$ as the exchange current density and $b_{ORR/MOR}$ as the Tafel slope of the respective reaction. $\tilde{\eta}$ is the difference between the ORR and MOR equilibrium potential. Since oxygen, C_{O_2}, is always available on the cathode, the cathode potential relaxes after CI immediately towards the ORR equilibrium potential; only limited by the charging process of the double layer capacity, C_{DL}. The solid line in Fig. 2a shows the

characteristics schematically. The increase of methanol concentration, C_{MeOH}, (red dotted line in Fig. 2a) occurs delayed leading to a minimum in the relaxation curve (blue dotted line in Fig. 2a, for interpretation of the references to colour in this figure, the reader is referred to the web version of this article) due to an incipient mixed-potential formation.

Even though the anode relaxation behaviour originates from a completely different mechanism, from a mathematical perspective it has the same structure. Assuming a constant parasitic current, $i_{parasitic}$, on the anode (due to side reactions or oxygen crossover) that has to be counterbalanced by the MOR, the anode overpotential, η_a, can be expressed by

$$C_{DL}\frac{\partial \eta_a}{\partial t} = i_{parasitic} - i^0_{MOR}C_{MeOH}(1-\theta_{CO})e^{\frac{\eta_a}{b_{MOR}}} \qquad (3)$$

where the time-dependent free Pt catalyst sites, $1-\theta_{CO}$, are taken into account. As long as the amount of CO blocking the catalyst sites, θ_{CO}, is small, which is normally the case at high anode overpotential, the anode potential will drop towards the MOR equilibrium potential after CI. Since at low anodic overpotential the bifunctional mechanism is insufficient, the Ru catalyst is not able to activate enough water to produce OH groups for further CO oxidation to CO_2. Thus, the surface coverage of CO increases and blocks the catalyst gradually. To counterbalance the parasitic current, the anode overpotential has to increase with increasing surface coverage (see Fig. 2b).

The characteristic time, $\Delta\tau$, of the minimum of the potential relaxation curve as well as the amplitude, $\Delta\eta$, is used for a qualitative analysis of the measured CI data.

2.3.3. MeOH-stripping voltammetry

The anode catalyst layer was additionally characterized by MeOH-stripping voltammetry. Further details in regards to this characterization technique can be found amongst others in [21]. The methanol flow (1 M) at the anode was set to 1.1 ml min^{-1} and the cathode was first purged with nitrogen for 30 min and then fed with hydrogen at a flow rate of 50 ml min^{-1}. The cell was set to a fixed voltage of 100 mV (vs. the hydrogen fed cathode side) under potentiostatic control for a period of 10 min to adsorb methanol on the active sites of the anode. The anode was then purged with water for 30 min to flush the non-adsorbed methanol while the cell was still under potentiostatic control at 100 mV. Finally, the stripping scan was recorded at 10 mV s^{-1} from 100 to 800 mV.

2.3.4. Cyclic voltammetry measurements

Cyclic voltammetry (CV) measurements were carried out according to [11]. The working electrode was first purged with water and then with nitrogen. The counter electrode was purged with nitrogen. Then, the working electrode was supplied with
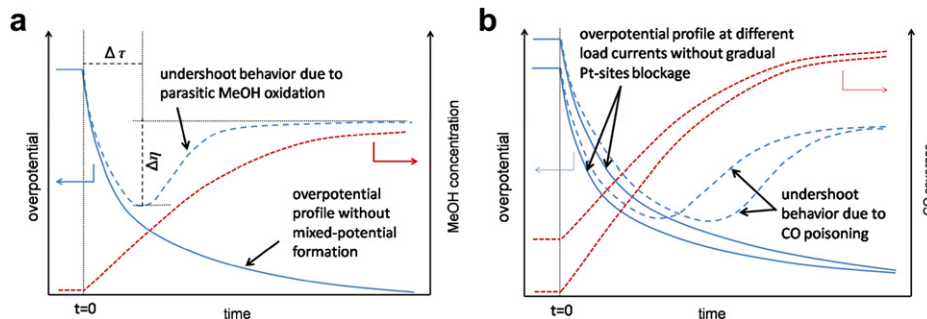

Fig. 2. Schematic of the potential relaxation curve after CI for (a) cathode overpotential due to parasitic MOR and (b) anode overpotential due to CO poisoning of the Pt-sites.
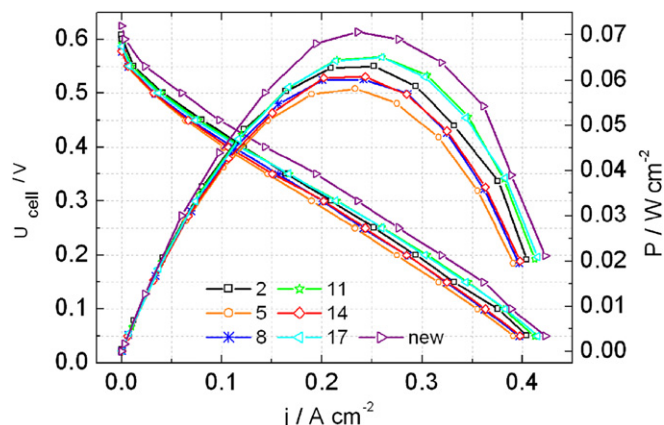
Fig. 3. U–j-curves and power density curves of the six aged MEA segments (2, 5, 8, 11, 14, 17) and the new MEA-segment measured in potentiostatic mode.

nitrogen with a flow rate of 300 ml min^{-1} and the counter electrode with 10 ml min^{-1} hydrogen for a period of 45 min. Then the voltage cycling was carried out from 0 V to 800 mV with a scan rate of 20 mV s^{-1}.

3. Results and discussion

3.1. Cell voltage and overpotential measurements

As expected, the new MEA shows the best U–j-curve, see Fig. 3. The performance difference in comparison to that of the aged MEA segments is in the range of 5–12 mW cm^{-2} at maximal power point. All aged segments show, in the activation controlled region, a steeper slope compared to the new MEA, while in the ohmic controlled region all slopes are nearly similar. This leads to a voltage decay of around 30–50 mV along the U–j-curve. A relationship between performance and thus degradation progress of the aged segments and their local position with respect to the flow distribution from methanol inlet (segment 17) to methanol outlet (segment 2) cannot be found.

More information about the origin of the measured voltage loss can be extracted from overpotential measurements. In this work, all overpotentials are represented by positive values while the electrodes are under load, independent of the electrode in which they occur. The anode and cathode overpotentials are defined in Eq. (1). Further, the ohmic losses originated by the proton migration within the membrane and the electrical resistance were subtracted from the measured overpotentials. Therefore, the high frequency resistance (HFR at 10 kHz) at a given current density measured
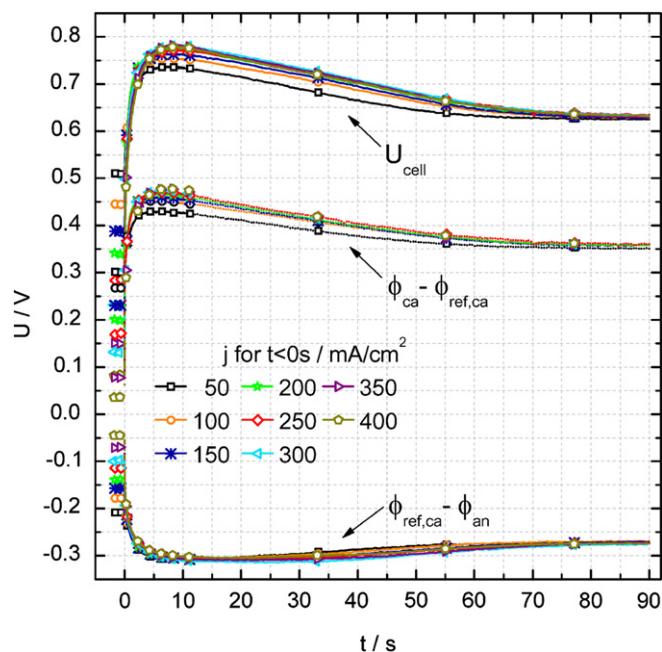

Fig. 5. Characteristic behaviour of the electrode potentials and the cell voltage for current interrupt measurements exemplary shown for the new MEA segment: cell voltage and cathode potential show an overshoot, anode potential shows an undershoot.

between the examined electrode to the reference electrode was used for the ohmic drop correction. Fig. 4 shows the anodic and cathodic overpotentials of all MEA segments.

The characteristics of the overpotential with current density can be summarized into three regions. At low current densities the overpotentials increase logarithmically corresponding to the activation controlled region. At moderate current densities, there is a linear increase due to dominating ohmic losses in the catalyst layers. Finally, at high current densities, a slightly more pronounced increase of the overpotentials due to mass transport losses can be observed, especially for the cathode overpotential. It is interesting to note that neither the anode nor the cathode overpotential of the new MEA segment shows a unique characteristics and both lie between the correspondent overpotential of the aged MEA segments. Again, there is no specific trend with respect to the flow pattern for the behaviour of the overpotentials of the long-term operated MEA segments from inlet to outlet. However, a correlation between the cathode and anode overpotential is observed for each segment in the manner that high anode overpotential implies low cathode overpotential and vice versa.
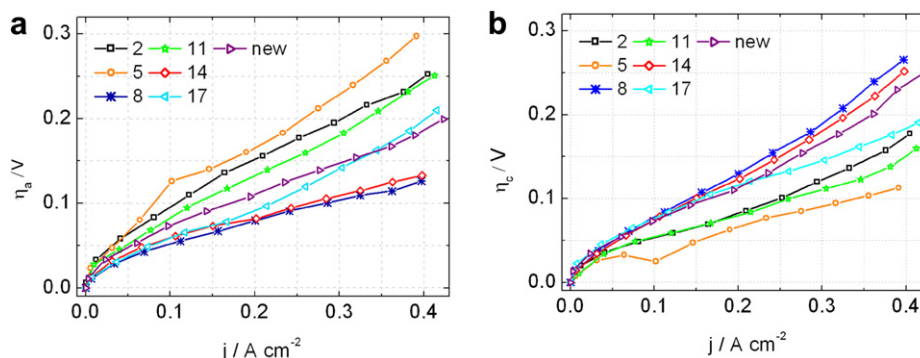

Fig. 4. (a) Anode and (b) cathode overpotential of the six long-term operated MEA segments (2, 5, 8, 11, 14, 17) and the new MEA-segment.
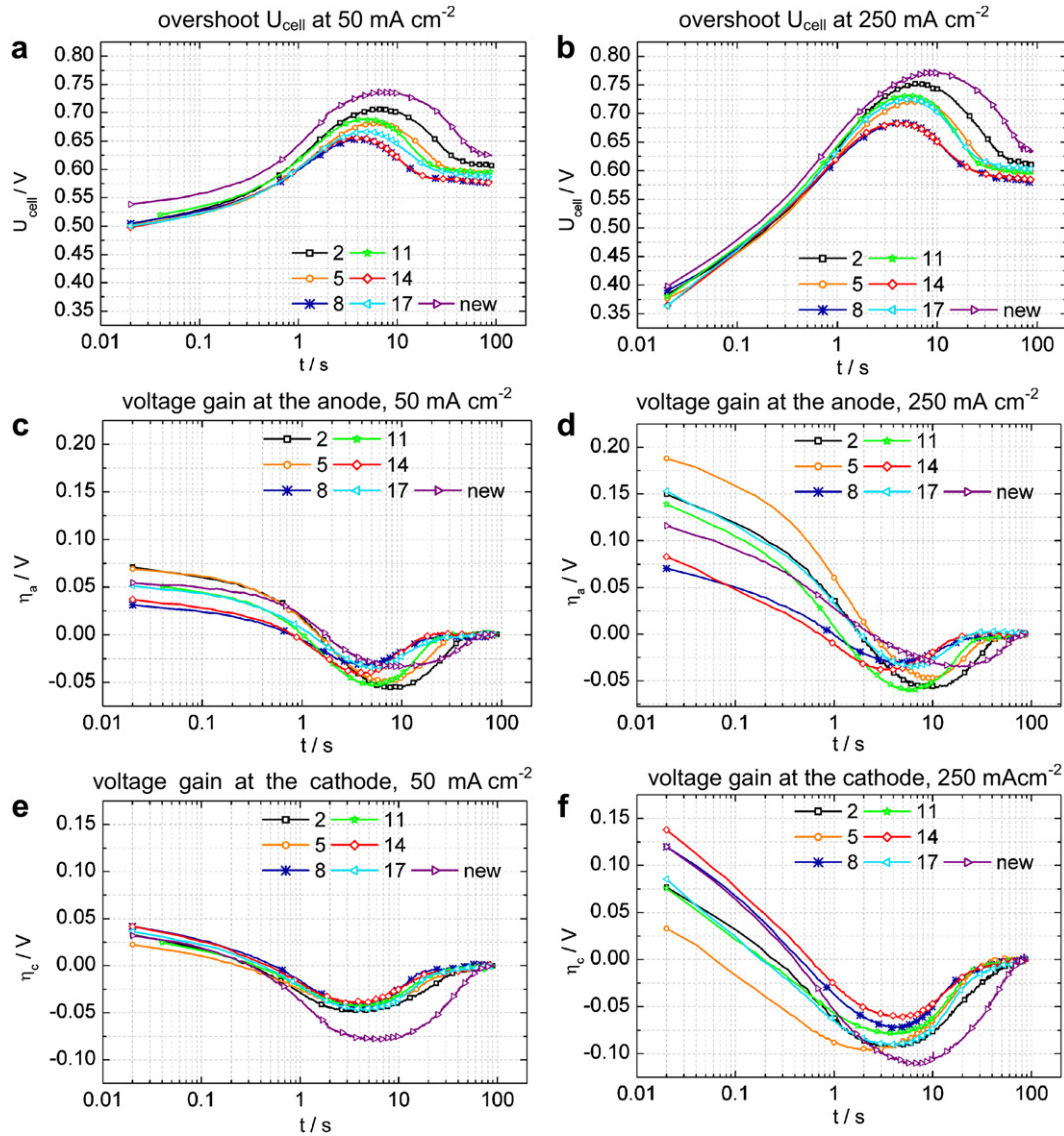
Fig. 6. Comparison of the current interrupt measurements of the 6 long-term operated MEA segments (2, 5, 8, 11, 14, 17) and the new segment. Methanol inlet: segment 17, methanol outlet: segment 2.

3.2. Current interrupt measurements

Fig. 5 shows the characteristic behaviour of the electrode potentials and the resulting cell voltage for the new MEA. It can be seen that the cell voltage shows an overshoot depending on the load current. This overshoot results from the dynamic response of

the cathode potential (around 70%) as well as the anode potential (around 30%).

The overshoot is more pronounced at higher load. However, the increase itself is decreasing with higher load. This is mainly attributed to the cathode relaxation. The cathode overshoot of the new segment is up to 127 mV high. It is reached after 6–8.2 s
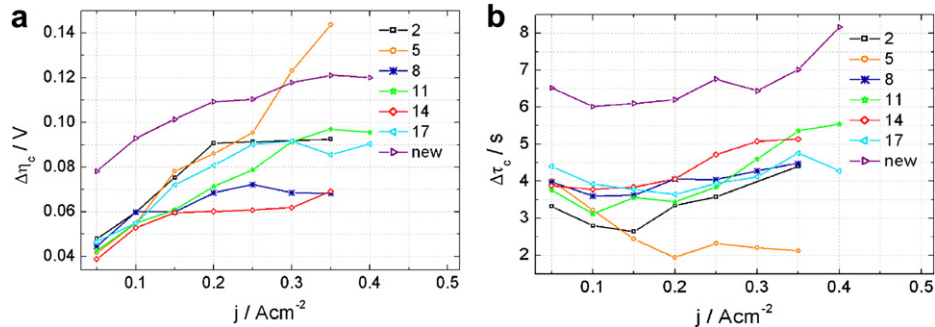

Fig. 7. Peak analysis of the temporary potential gain at the cathode $\Delta\eta_c$ after CI at different current density values. (a) Maximum of the short term voltage gain at the cathode $\Delta\eta_c$. (b) Time elapsed $\Delta\tau_c$ after opening the external circuit till $\Delta\eta_c$ is reached.
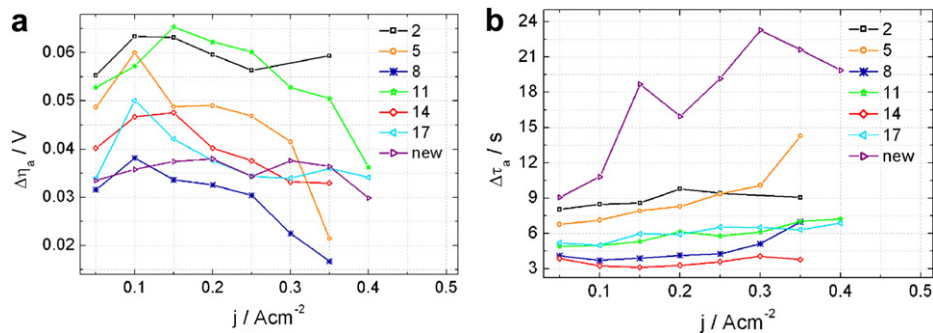
Fig. 8. Peak analysis of the temporary potential gain at the anode during current interrupt measurements as a function of load current density. (a) Maximum of the voltage gain at the anode ($\Delta\eta_a$). (b) Time after CI ($\Delta\tau_a$) until $\Delta\eta_a$ is reached.

depending on the load current density. The undershoot of the anode reaches a maximum of 38 mV after 9–23 s. The over-/undershoot of the electrodes led to an improved cell performance for a short time. Furthermore, the cell voltage of the steady-state operating points at $t < 0$ is consistent with the measured polarization curve. The CI measurements for the new MEA segment are compared against the six aged MEA segments (2, 5, 8, 11, 14, 17) at two representative current densities, 50 and 250 mA cm^{-2}. In this work, the voltage loss is defined as a positive value and the voltage gain is defined as a negative value regardless of the electrode in which these losses/gains occur. Hence, the temporarily appearing voltage gains at the electrodes are represented by an undershoot. This temporary voltage gain is calculated according to the following equations

$$\eta_a = \left(\phi_{a,t} - \phi_{ref,c}\right) - \left(\phi_{a,t=90s} - \phi_{ref,c}\right) \tag{4}$$

$$\eta_c = \left(\phi_{c,t=90s} - \phi_{ref,c}\right) - \left(\phi_{c,t} - \phi_{ref,c}\right) \tag{5}$$

It is assumed that the electrode potentials reached steady-state after 90 s ($\varphi_{a,t=90s}$ and $\varphi_{c,t=90s}$). The overshoot in the cell voltage of the long-term operated segment is smaller in comparison to that of the new MEA segment, as illustrated in Fig. 6a and b for a load current density of 50 mA cm^{-2} and 250 mA cm^{-2}. This is mainly due to smaller voltage gains at the cathode. Further, the maxima/minima of the over-/undershoots of the cell voltage and the anode and cathode overpotentials of the aged segments appear earlier than that of the new cell. The maxima of the potential gains at the cathode of the aged segments are all reached after similar times. Only segment 5 is an unexplained exception at $j > 150$ mA cm^{-2}. The minima of the anode undershoots of the aged segments appear at different times. Hence, they determine the time sequence of the

cell voltage overshoots although they are much smaller than the cathode overshoots. Again, no observable trend is recorded for the current interruption among the aged segments between methanol inlet (segment 17) and methanol outlet (segment 2).

The temporary potential gain measured at the cathode is consistent with the theoretical explanations of the previous section and can be related to membrane or cathode catalyst layer degradation.

Fig. 7 shows the results of the peak analysis of the cathode potential relaxation curves. The maximum of the voltage gain at the cathode increases with increasing current density with an asymptotical characteristic. This is consistent with the theory described in Section 2.3.2. The higher current density leads to a lower methanol concentration at the phase boundary anode catalyst layer/membrane. This, of course, is accompanied with a lower methanol crossover through the membrane. Considering that the methanol crossover decreases with increasing current density, more time is required for the MOR at the cathode side to measure an influence after CI. Hence, the maximum of the temporary cathode voltage gain increases with increasing current density and by trend the maximum is observed.

The maximum of the voltage gain at the cathode of the aged segments depends on the current density and has been measured to be around 18.6 and 52.8 mV smaller than that for the new segment. This maximum is reached between 1.4 and 3.9 s faster than that of the new MEA depending on the current density. One explanation for these differences could be that methanol crosses the membrane of the aged segments faster. This in turn leads to the conclusion that the membrane is degraded by membrane thinning, as Nafion® is slightly soluble in methanol, or by structural changes of the membrane towards wider pores. Further, the results could also be a hint for a degraded cathode catalyst layer as a more methanol-tolerant cathode would be more stable with respect to
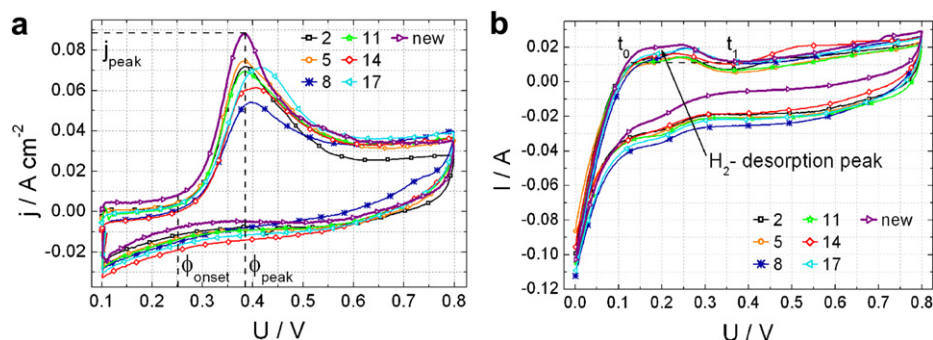

Fig. 9. Results of (a) the methanol stripping experiments and (b) cathode cyclovoltammetry measurements including an illustration of the parameters used for peak analysis exemplary shown for the new MEA segment.

Table 2
Extracted parameters obtained from the cyclic voltammetry measurements.

CCM	φ_{onset}/V	φ_{peak}/V	j_{peak}/A cm^{-2}	Q_{des}/C
New	0.256	0.380	0.088	0.072
2	0.266	0.386	0.072	0.055
5	0.264	0.382	0.075	0.058
8	0.274	0.398	0.054	0.051
11	0.262	0.385	0.069	0.052
14	0.270	0.404	0.061	0.038
17	0.272	0.416	0.072	0.054

Fig. 11. Cross-sectional SEM pictures of (a) the long-term operated MEA segments 2, (b) new segment after breaking under liquid N_2.

the parasitic MOR. That means the exchange current density of the new segment would be larger than that of the aged segments. More methanol must reach the cathode before the parasitic reaction of MOR at the cathode gets enough influence to prevent a further increase of the cathode potential. This also results in a more pronounced $\Delta\eta_c$ as well as a delayed appearance of the maximum of the new segment compared to the aged segments. The lower exchange current density of the long-term operated MEA segments means less reaction sites per geometric area or less catalyst activity. The reasons are possible structural changes or catalyst loss within the electrode, caused through, for instance, catalyst particle growth or electrochemical corrosion of the carbon support. As will be seen later, comparing the EDX analysis of the aged segment 5 with the new segment shows significantly lower fluorine and oxygen peaks in the catalyst layer of the cathode, see Fig. 10. Especially the lower fluorine peak indicates electrolyte dissolution within the cathode catalyst layer, which leads to reduced coupling between the electrolyte and electron phase. Comparing the long-term operated segments with respect to the flow field pattern, there is again no trend from methanol inlet to methanol outlet.

Fig. 8 shows the results of the peak analysis of the anode undershoot. The maximum of the temporary voltage gain at the anode first increases with current density (up to 150–200 mA cm^{-2}) and then it decreases. By trend, the maximum is reached later with increasing current density. There is no trend observable among the 6 long-term operated segments between methanol inlet (segment 17) and methanol outlet (segment 2). Obviously, the maximum $\Delta\eta_a$ of the new segment occurs later compared to the old ones. According to the theory devised, this implies that the anode of the new MEA segment shows a higher activity towards CO oxidation, due to a more sufficient bi-functional mechanism. This is an indicator for either higher ruthenium content or at least finer distributed ruthenium particles in the anode catalyst layer.

3.3. Cyclic voltammetry

Methanol stripping and cathode cyclic voltammetry measurements are carried out to further investigate the catalyst layers of the
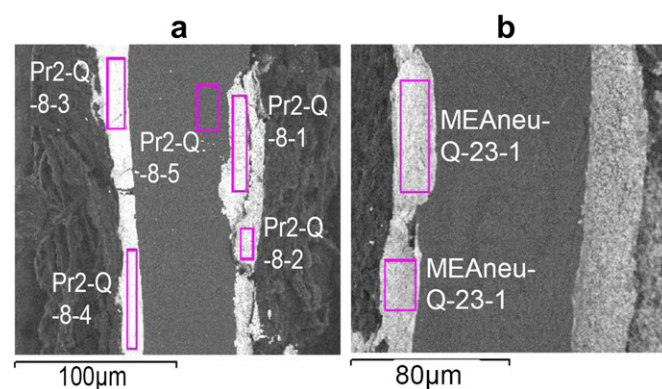
MEAs. The first cycle of the methanol stripping curves of the aged and new anodes are shown in Fig. 9a. All curves show the current density peak that is caused by the oxidation of previously absorbed methanol and methanol intermediates. Analysis of the peak current density, j_{peak}, peak potential, φ_{peak}, and onset potential, φ_{onset}, was done to quantify the degradation at the anode.

It can be said that the higher the peak current density, the lower the onset and peak potential are. Similarly, the narrower the peak width, the better the activity of the anode catalyst layer towards methanol oxidation is. The peak current density and the peak potential can be easily obtained from the measured curve. The onset potential is defined by the potential where a certain slope of the curve is exceeded.

The cathode cyclic voltammetry measurements were carried out to investigate the H_2 desorption peak (see Fig. 9b), which is normally a measure for the real active surface area. As these DMFC MEAs have Pt/Ru as anode catalyst, it cannot be excluded that fractions of ruthenium moved to the cathode side during operation. Since ruthenium influences the Pt-specific H_2 desorption peak, it is not possible to determine quantitatively the active area via the H_2 desorption peak. Piela et al. [22] showed that the H_2 desorption peak is smaller with a Pt/Ru cathode catalyst compared to a pure Pt catalyst. A significant change in the H_2 desorption peak after 110 h of DMFC operation was also found by Wang et al. [23] and explained by the deposition of Ru, which crosses from the anode over to the cathode. Thus, we use the charge under the H_2 desorption peak as an indication for Ru crossover and compare the six aged segments with the new segment qualitatively, by keeping in mind that degradation affects Pt distribution and the carbon support could affect the CV data.

Table 2 shows the extracted parameters of all MEAs. It can be concluded that the new MEA shows the best values for all
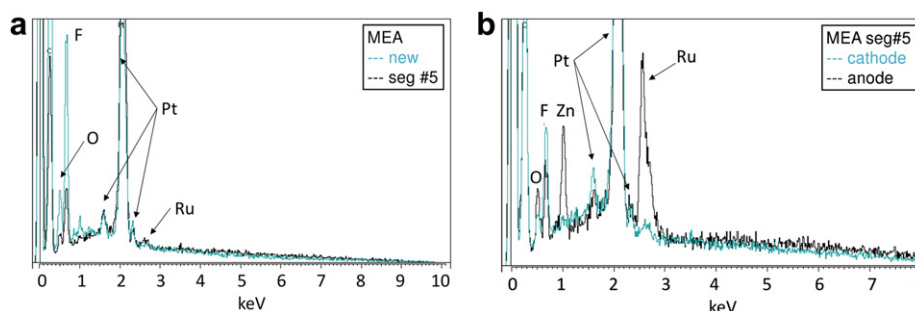

Fig. 10. (a) EDX analysis of the cathode catalyst layer of the new MEA and the long-term operated MEA segment 5 after breaking under liquid N_2. (b) Comparison of the anode/cathode catalyst layer of MEA segment 5.

Table 3
Matrix of the extracted parameters for all investigated segments.

	φ_{onset}	j_{peak}	Q_{des}	η_a	η_c	$\Delta\eta_a$	$\Delta\tau_a$	$\Delta\eta_c$	$\Delta\tau_c$
φ_{onset}	1.00	−0.85	−0.72	−0.56	0.32	−0.36	−0.83	−0.73	−0.37
j_{peak}	−0.85	1.00	0.83	0.61	−0.31	0.32	0.87	0.85	0.27
Q_{des}	−0.72	0.83	1.00	0.46	−0.19	0.11	0.89	0.83	0.21
η_a	−0.56	0.61	0.46	1.00	−0.90	0.72	0.29	0.77	−0.45
η_c	0.32	−0.31	−0.19	−0.90	1.00	−0.51	0.02	−0.63	0.72
$\Delta\eta_a$	−0.36	0.32	0.11	0.72	−0.51	1.00	0.07	0.24	−0.16
$\Delta\tau_a$	−0.83	0.87	0.89	0.29	0.02	0.07	1.00	0.72	0.48
$\Delta\eta_c$	−0.73	0.85	0.83	0.77	−0.63	0.24	0.72	1.00	−0.19
$\Delta\tau_c$	−0.37	0.27	0.21	−0.45	0.72	−0.16	0.48	−0.19	1.00

parameters. The values of the degraded MEAs reveal among each other no correlation with respect to their local position.

3.4. SEM/EDX analysis

The EDX analysis confirms a small ruthenium content in the cathode catalyst layer of the aged segments whereas ruthenium was not detected in the cathode catalyst layer of the new MEA as given in Fig. 10. The low fluorine peak measured for the old segments can be interpreted as a sign of electrolyte dissolution within the catalyst layer. The SEM pictures of the MEA cross-sections in Fig. 11 show that the thickness of the catalyst layers varies significantly. Further, the catalyst layers of the long-term operated MEAs are quite brittle compared to the new MEA. It is quite conceivable that these micro structural changes dominate all previous mentioned results and mask the existence of a local degradation level.

3.5. Cross correlation

In this work, several characterization methods were used to analyze MEA degradation, revealing quantitative values that could be related to each other. In Table 3, we devise a correlation coefficient between the extracted parameters of all investigated MEA segments. Setting a conservative value of ±0.7 for having an actual correlation between a pair of parameters, the following parameters stand out: φ_{onset}, j_{peak}, Q_{des}, $\Delta\tau_a$, $\Delta\eta_c$.

The correlation coefficient, cc, of e.g. φ_{onset} and j_{peak} has a negative value of −0.85. This means, the MEA with a low onset potential shows a high peak current for the MeOH-stripping experiment. Additionally, the cathode shows a large H_2 desorption area (cc = −0.72) for the CV. Furthermore, the characteristic time constant for the anode relaxation of this MEA is large (cc = −0.83) and so is the amplitude of the cathode potential gain (cc = −0.73). These correlations could be interpreted by a different state of ruthenium dissolution in the anode and migration to the cathode for the aged MEAs. An MEA with high ruthenium content, well dispersed, will have a low onset potential, high peak current and a large characteristic time constant for the anode undershoot. In case the ruthenium has dissolved and migrated to the cathode, this will suppress the H_2 desorption peak and make the cathode potential less stable against the parasitic MOR, leading to a decreased cathode overshoot. The missing correlation of characteristic time constant for the cathode undershoot can be explained by the fact that these values are all close together and thus not a proper criteria for the degradation analysis. The same can be said for the maximum of the anode undershoot, since this value is less pronounced than for the cathode undershoot.

4. Conclusion

In-situ electrochemical investigations were conducted on a long-term operated DMFC MEA of technical size. In order to locally analyze the degradation level of this MEA, caused by inhomogeneous educts and product concentrations and temperature distributions on the active area during operation in a fuel cell stack, the MEA was segmented into small pieces and separately characterized in a small test cell with reference electrodes. For the investigated MEA it was found that the aging process of the MEA was independent of the local position within the stack. Comparing the overpotential curve of a new MEA segment as a benchmark with the long-term operated ones, small performance losses were observed. Current interrupt measurements, MeOH-stripping experiments and cyclicvoltammety measurements indicate that one reason for this performance loss is the loss of catalyst activity inside the anode and cathode catalyst layers due to Ru dissolution and migration. These results are confirmed by EDX analysis of the cathode catalyst layer of the aged segments. Additionally, electrolyte dissolution within the catalyst layer is detected. Finally, SEM analysis shows brittle catalyst layers with inhomogeneous thickness for the aged MEAs. The degradation processes within the fuel cell are highly influenced by the operating conditions and therefore our findings are not general.

References

[1] George A. Olah, Alain Goeppert, G.K. Surya Prakash, Second Updated and Enlarged Edition, Wiley-VCH, 2009.
[2] G. Jerkiewicz, G. Vatankhah, J. Lessard, M.P. Soriaga, Y.S. Park, Electrochimica Acta 49 (2004) 1451–1459.
[3] H. Xu, R. Kunz, J.M. Fenton, Electrochemical and Solid-State Letters 10 (2007) B1–B5.
[4] C.H. Paik, T.D. Jarvi, W.E. O'Grady, Electrochemical and Solid-State Letters 7 (2004) A82–A84.
[5] C. Eickes, P. Piela, J. Davey, P. Zelenay, Journal of the Electrochemical Society 153 (2006) A171–A178.
[6] C.Y. Du, T.S. Zhao, W.W. Yang, Electrochimica Acta 52 (2007) 5266–5271.
[7] P. Zelenay, Y.S. Kim, R. Bashyam, J.-H. Choi, ECS Transactions 1 (2006) 437–445.
[8] P. Piela, C. Eickes, E. Brosha, F. Garzon, P. Zelenay, Journal of the Electrochemical Society 154 (2004) 739–744.
[9] J.-H. Choi, Y.S. Kim, R. Bashyam, P. Zelenay, ECS Transactions 1 (2006) 437–445.
[10] W.M. Chen, G.Q. Sun, J.S. Guo, X.S. Zhao, S.Y. Yan, J. Tian, S.H. Tang, Z.H. Zhou, Q. Xin, Electrochimica Acta 51 (2006) 2391–2399.
[11] H.-C. Cha, C.-Y. Chen, J.-Y. Shiu, Journal of Power Sources 192 (2009) 451–456.
[12] C.-C. Hung, P.-Y. Lim, J.-R. Chen, H.C. Shih, Journal of Power Sources 196 (2011) 140–146.
[13] J.-Y. Park, M.A. Scibioh, S.-K. Kim, H.-J. Kim, I.-H. Oh, T.G. Lee, H.Y. Ha, International Journal of Hydrogen Energy 34 (2009) 2043–2051.
[14] Z. Siroma, N. Fujiwara, T. Ioroi, S. Yamazaki, K. Yasuda, Y. Miyazaki, Journal of Power Sources 126 (2004) 41–45.
[15] J. Wu, X.Z. Yuan, J.J. Martin, H. Wang, J. Zhang, J. Shen, S. Wu, W. Merida, Journal of Power Sources 184 (2008) 104–119.
[16] F.N. Büchi, M. Inaba, T.J. Schmidt, Springer (2009).
[17] W. Chen, G. Sun, J. Guo, X. Zhao, S. Yan, J. Tian, S. Tang, Z. Zhou, Q. Xin, Electrochimica Acta 51 (2006) 2391–2399.
[18] D. Dixon, K. Wippermann, J. Mergel, A. Schoekel, S. Zils, C. Roth, Journal of Power Sources 196 (2011) 5538–5545.
[19] D. Gerteisen, Journal of Applied Electrochemistry 37 (2007) 1447–1454.
[20] D. Gerteisen, Journal of Power Sources 195 (2010) 6719–6731.
[21] M. Carmo, V.A. Paganin, J.M. Rosolen, E.R. Gonzalez, Journal of Power Sources 142 (2005) 169–176.
[22] P. Piela, C. Eickes, E. Brosha, F. Garzon, P. Zelenay, Journal of the Electrochemical Society 151 (2004) A2053–A2059.
[23] Z.-B. Wang, H. Rivera, X.-P. Wang, H.-X. Zhang, P.-X. Feng, E.A. Lewis, E.S. Smotkin, Journal of Power Sources 177 (2008) 386–392.